Analysis and Design of Antimisalignment IPT System through Auxiliary Coil Position Reconstruction for Electric Bicycle Applications

Peng Gu, *Member, IEEE*, Mingda Gao, Xianrui Zeng, Shibo Wang, and Yijie Wang, *Senior Member, IEEE*

***Abstract*—In this article, a wireless charging system architecture is proposed and designed to charge the receiving coil installed on the hollow frame of the electric bicycle (EB) body through the cylindrical charging coils on both sides. Among them, the size of the transmitting coils is designed and optimized to enhance tolerance to three-dimensional misalignment. A novel auxiliary coil position reconstruction (ACPR) method is proposed to actively offset the misalignment effect by adjusting the position of an auxiliary coil nested on the primary coil. The parameters of the resonant network are reconstructed by adjusting the position of the auxiliary coil when the EBs are parked in a misaligned state. The topology enables the voltage reconstruction of an equivalent T/S constant voltage topology, even effectively eliminating the voltage variation caused by the misalignment with simply moving the auxiliary coil. A prototype of the proposed system is built. The misalignment tolerance against output voltage changes in different dimensions is verified through the proposed ACPR method, efficiency of the system is demonstrated to be maintained at around 90%.**

***Index Terms*—Auxiliary coil position reconstruction, electric bicycle application, equivalent compensation topology, magnetic coupling structure design, wireless charging.**

I. Introduction

WIRELESS charging for various devices through inductive power transfer (IPT) technology greatly facilitates the energy supply process [1], [2]. IPT technology has been widely applied in fields of transportation electrification [3], [4], [5], [6], smart grids [7], [8], [9], and consumer electronics [10], [11], [12]. Among them, electric bicycles (EBs) are convenient for short-distance urban transportation due to their exquisite structure and functions. EBs have a broad application market around the world. However, outdoor charging equipment is usually connected to the EBs through wires. Aging lines, rain, or snow weather make short circuit faults occur frequently in the news, and the resulting fires cause huge losses [13]. Therefore, it is necessary to design wireless charging solutions for EBs to avoid the above safety hazards.

Scholars have done relevant work on wireless charging solutions for electric bicycles. A closely coupled lumped magnetic coupler configurations installed within or around a kickstand of an EB was proposed in [14]. The proposed scheme is experimentally proven to have a misalignment tolerance of ±20-mm range. A coil tuning mechanism was implemented to suppress the reverse current in the wireless charger, and a linear closed-loop control mechanism was proposed to effectively regulate the output voltage of the EB in [15]. A double coupled wireless fleet charging system for electric bicycles to provide individual control of each charging bicycle location using an intermediary coupler was proposed in [16] to prevent magnetic radiation into the environment. An IPT system based on variable coil structure was proposed in [17] to charge EBs. A method for EB wireless charging by a hybrid topology with two ac switches was proposed in [18]. The constant voltage (CV)/constant current (CC) mode of the wireless charging system was switched by adjusting the ON–OFF status of the switches. The position of the receiving coil of the EBs wireless charging system was analyzed in [19] to achieve better efficiency, and a simple but robust control method was proposed in this article. A hybrid topology with two ac switches and an additional capacitor at receiving circuit was proposed in [20], the characteristics of CC output and CV output were obtained by switching the switches for *CLC-LCL* topology to *CLC* topology. In short, most relevant research on wireless charging technology for electric bicycles focuses on the two aspects of adaptive magnetic coupling structure design and charging mode CC/CV switching. Since the parking state of an electric bicycle is uncertain, it is difficult to align the receiving side of the EB body and the transmitting side of the charging device, and the existing research on misalignment tolerance is not significant [14]. In this way, it is necessary to improve the misalignment tolerance of EB wireless charging systems

Received 6 July 2025; revised 24 August 2025; accepted 23 September 2025. Date of publication 30 September 2025; date of current version 19 January 2026. This work was supported in part by the National Natural Science Foundation of China under Grant 52307005, in part by China Postdoctoral Science Foundation under Grant 2023TQ0052, in part by Postdoctoral Fellowship Program of China Postdoctoral Science Foundation under Grant GZC20230386, in part by Fundamental Research Funds for the Central Universities under Grant N2404016, and in part by Young Elite Scientist Sponsorship Program by Chinese Society for Electrical Engineering under Grant CSEE-YESS-2023008. Recommended for publication by Associate Editor K. Ngo. *(Corresponding author: Peng Gu.)*

Peng Gu, Mingda Gao, and Shibo Wang are with the College of Information Science and Engineering, Northeastern University, Shenyang 110819, China. (e-mail: gupeng@ieee.org; 20215410@stu.neu.edu.cn; 2371012@stu.neu.edu.cn).

Xianrui Zeng is with the School of Electrical Engineering and Automation, Harbin Institute of Technology, Harbin 150001, China, and also with the Institute of Spacecraft System Engineering, China Academy of Space Technology, Beijing 100094, China (e-mail: xianruizeng@alu.hit.edu.cn).

Yijie Wang is with the School of Electrical Engineering and Automation, Harbin Institute of Technology, Harbin 150001, China (e-mail: wangyijie@hit.edu.cn).

Color versions of one or more figures in this article are available at https://doi.org/10.1109/TPEL.2025.3616186.

Digital Object Identifier 10.1109/TPEL.2025.3616186

through the design of inductive couplers and network topology based on the morphological characteristics of EBs and parking spaces.

The influence of the mechanical frame has been considered in the process of wireless charging in some conditions. The metal influence on the wheel hub of the electric vehicle was weakened by placing a ferrite core in [21]. A nonmetallic EB wheel material was used to receive energy through the front wheel of the EB while eddy current losses were avoided as much as possible in [22]. Besides, in other fields of wireless charging systems for transportation vehicles, the influence of mechanical frames on the systems has also been minimized or ignored to the greatest extent [23], [24], [25], [26].

It is an effective solution to improve the misalignment tolerance of wireless charging systems through the design of magnetic coupling structures according to different shapes of electrical devices. For electric vehicle wireless charging applications, planar-shaped magnetic coupling structures were proposed to improve misalignment tolerance [27]. On the basis of the traditional DD-shaped coil and planar solenoid magnetic coupling structure with misalignment tolerance, scholars have made corresponding improvements to further enhance the misalignment tolerance according to the space characteristics between the electric vehicle chassis and the charger during parking wireless charging [28], [29]. In this article, EBs are the object of research. It is necessary to make adaptive designs based on the characteristics of EBs parking and charging. A concentrated magnetic flux asymmetric magnetic coupling structure was proposed in [30]. A method to concentrate the magnetic flux and weaken the demagnetization coefficient through the ferrite core shaft was proposed in [31]. An I-shaped magnetic coupling structure was designed in [32] to further concentrate the magnetic flux and reduce the output side fluctuation. A cubic magnetic coupler was proposed in [33] that takes into account both the wide air gap capability and strong misalignment tolerance for IPT. The wireless charging device in [34] emits a magnetic field through bar coils and had rotational misalignment capabilities for autonomous underwater vehicle applications. It can be known from the above work that the three-dimensional tube-shaped magnetic coupling structure has excellent ability to concentrate magnetic flux. Combined with the frame structure of electric bicycle parking, the transmitting coil can be designed into a cylindrical structure to concentrate the magnetic flux and tolerate misalignment. For the receiving coil, the power was received by assembling the coil in the hollow frame part of the electric bicycle.

In order to further improve the misalignment tolerance, scholars use theoretical derivation to optimize topological parameters to achieve dislocation tolerance. In [35] and [36], the conditions that the output voltage or current is insensitive to the coupling coefficient and the load resistance were found through modeling and mathematical derivation methods. A family of hybrid IPT topologies was proposed to achieve a near load-independent output and high misalignment tolerance for an IPT system in [37]. The above methods of suppressing output fluctuations through topological parameter design can reduce rather than eliminate fluctuations. Therefore, it is necessary to eliminate the output changes caused by changes in the mutual inductance of the primary and secondary sides by reconstructing the topological parameters of the resonant network. A method to achieve a wider range of misalignment tolerance through switching modes was proposed in [38]. The scholars realize the reconstruction of system parameters through switches to extend the coupling range, which is worthy of reference.

Based on the recent researches, a solution to achieve high misalignment tolerance wireless charging through the hollow frame of the electric bicycle body and parking stands is proposed in this article. In addition, by proposing a novel auxiliary compensation coil with a reconfigurable position, an adjustable degree of freedom is added to counter the changes in mutual inductance during the misalignment process. The main contributions of this article are summarized as follows:

1) An IPT system architecture is proposed to wirelessly charge the receiving coil assembled in the EB hollow frame through the cylindrical charging coils on both sides.
2) The magnetic coupling structure is analyzed, designed, and optimized to improve the misalignment tolerance.
3) Most importantly, an ACPR method is proposed to actively offset the misalignment effect by adjusting the position of the auxiliary coil and reconstructing the system parameters. In this way, the misalignment tolerance of the IPT system is fundamentally enhanced.

The rest of this article is organized as follows. The wireless charging magnetic coupling structure is designed and the parameters are optimized using finite element simulation in Section II. In Section III, the circuit topology of the proposed IPT system after adding the auxiliary coil is analyzed, and the design process of the auxiliary coil is illustrated. An experimental prototype is built and the experimental conclusions are verified in Section IV. Finally, Section V concludes this article.

II. Magnetic Coupling Structure Design and Optimization

A. Proposal of System Architecture and Magnetic Coupling Structure

An IPT system with simple structure, high integration, and strong misalignment tolerance is proposed in this article for application in the energy supply of EBs. The installation position of the receiving coil should be considered because of the electric bicycle structure. A charging structure suitable for the hollow area on the vehicle body is proposed in this article, and the installation position of the receiving coil can be integrated in A, B, or C position of an EB, as shown in Fig. 1. The transmitting coils mounted on the bicycle parking bracket are arranged coaxially with the receiving coil and placed symmetrically on both sides of receiving coil.

Based on the abovementioned system architecture, the shape and size of the transmitting coils and receiving coil need to be determined first. In order to effectively validate the proposed charging antimisalignment mechanism and facilitate modeling and analysis, the receiving coil in this study is designed as a cylinder with a diameter of 400 mm and a height of 50 mm. The selected size ensures sufficient coupling area and can better show the impact of the charging structure layout on the transmission performance. In practical applications, the coil dimensions can

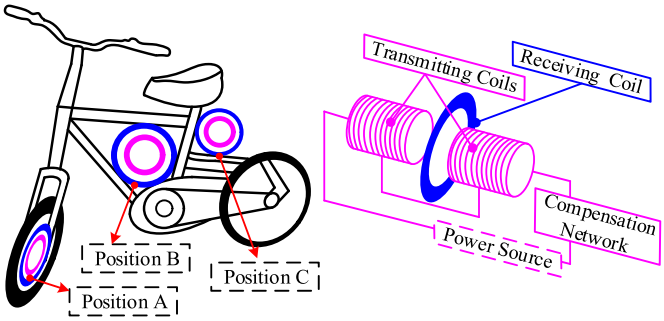

Fig. 1. Proposed EBs wireless charging system architecture.

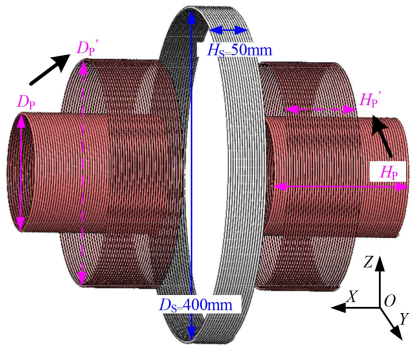

Fig. 2. Simulation model of the magnetic coupler and key design parameters.

be flexibly adapted to the specific geometry of the vehicle frame and the available cavity space. To enhance the concentration of the magnetic flux, improve the coupling coefficient, and increase misalignment tolerance, the transmitting coupler is configured as two tubular solenoid coils connected in series and positioned within the parking bracket. The magnetic coupling structure of the proposed IPT system is shown in Fig. 2.

B. Optimization of the Magnetic Coupling Structure on the Transmitter Side

According to the magnetic coupling structure in Fig. 2, three kinds of misalignment occur during EB charging: 1) the lateral misalignment Δx, 2) the longitudinal misalignment Δy, and 3) rotation angle misalignment $\Delta\alpha$.

In this section, the effects of three kinds of misalignment on the IPT system are improved by optimizing the parameters of the transmitting coils. In order to ensure a fair comparison, the amount of copper used in the transmitting coils are kept constant and its diameter D_P is optimized. Moreover, under the constraint of a fixed amount of copper, the corresponding coil height will shorten as the transmitting coil diameter D_p expands to D_p', as shown in Fig. 2. Practical engineering factors are taken into consideration, and excessive coil height is not conducive to integration. However, an excessively large coil diameter will also have a magnetic field effect on the surrounding environment. Therefore, to facilitate integration in public places and minimize the system's magnetic field effects on the environment, the D_P range is restricted to 140 mm–350 mm.

The mutual inductance value M_{PS} between the transmitting coils and the receiving coil is analyzed in ANSYS Maxwell by the finite element method (FEM). In order to intuitively reflect the impact of the above misalignment, the mutual inductance retention rate ΔM_{PS} is defined as

$$\Delta M_{PS} = \frac{M_{change}}{M_0} \times 100\% \tag{1}$$

M_{change} is the value in the misalignment situation, and M_0 is the value in the alignment situation.

The simulated mutual inductance value M_{PS} changes with Δx, as shown in Fig. 3(a). As the misalignment distance Δx increases, the mutual inductance M_{PS} gradually increases. Therefore, ΔM_{PS} generally shows an upward trend. In addition, as the diameter of the transmitting coil increases, the changing trend of ΔM_{PS} becomes more obvious. It is worth mentioning that when $D_P = 140$ mm, compared with the alignment situation, the variation range of ΔM_{PS} is less than 4%. The excellent lateral misalignment tolerance of the magnetic coupling structure in the *X*-direction is demonstrated.

The simulated mutual inductance value M_{PS} changes with $\Delta\alpha$, as shown in Fig. 3(b). It can be seen that the angular misalignment trend is consistent with the lateral misalignment trend. Similarly, as the diameter of the transmitting coil increases, the mutual inductance value M_{PS} gradually increases. Compared with Fig. 3(a), the change in ΔM_{PS} is less significant. In addition, when $D_P = 140$ mm, the ΔM_{PS} change is within 3.5%, which has excellent angle misalignment tolerance.

The misalignment in the *Y*-direction is shown in Fig. 3(c). In actual parking situation, the parking rack can be equipped with baffles to limit the parking position of EB. Therefore, only the case of Δy>0 is considered. It can be seen from the figure that the change trend is different from the above two cases in Fig. 3(a) and (b), the change of ΔM_{PS} in *Y*-direction is the most obvious. As Δy increases, ΔM_{PS} changes slowly at first. When Δy is greater than 80 mm, ΔM_{PS} decreases rapidly. When the diameter D_P is $D_{P1} = 140$ mm, the coupler still has a high misalignment tolerance. In summary, considering the mutual inductance change under the three misalignment states, D_P is designed as 140 mm

$$\boldsymbol{\Phi} = \boldsymbol{BS}. \tag{2}$$

The magnetic field transmission path for Δy = 160 mm is derived through the FEM to further investigate the impact of misalignment in the *Y*-direction on the magnetic coupling structure, as shown in Fig. 4. It can be seen from formula (2) that magnetic flux is related to magnetic flux density and area. In the alignment situation, the magnetic coupling structure has a uniform magnetic field, as shown in Fig. 4(a). Fig. 4(b) is in misalignment of the *Y*-direction, and the effective area for magnetic field propagation is reduced. Therefore, the coupling strength between the transmitting coils and the receiving coil is reduced. In addition, when the diameter of the transmitting coils is smaller, the effective area is less diminished, and the tolerance for misalignment is increased.

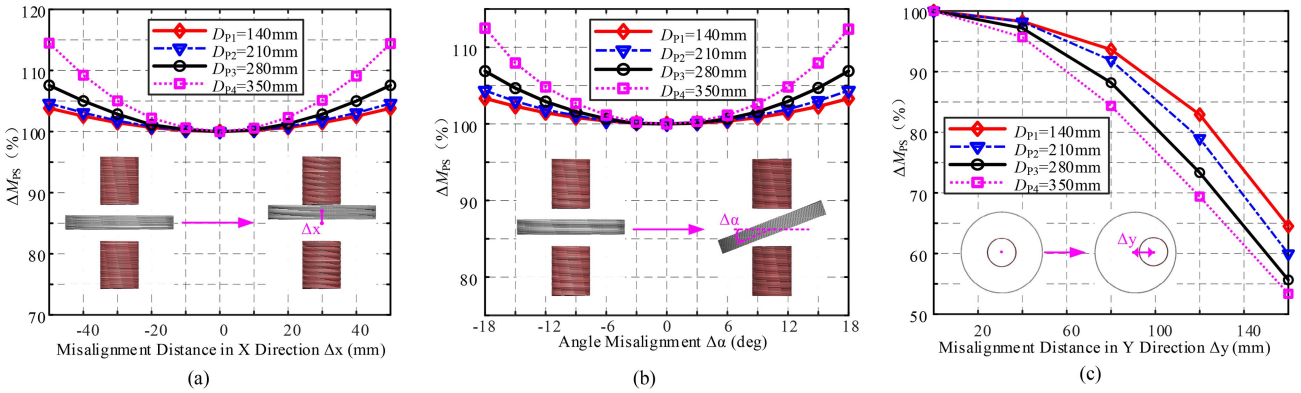

Fig. 3. Optimization of magnetic coupling structure parameters. (a) Mutual inductance between the transmitting coils and the receiving coil under the *X*-direction misalignment. (b) Mutual inductance between the transmitting coils and the receiving coil under the angle misalignment. (c) Mutual inductance between the transmitting coils and the receiving coil under the *Y*-direction misalignment.

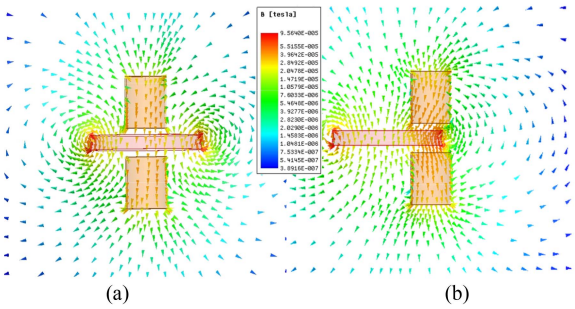

Fig. 4. Magnetic vector plot in the *Y*-direction on transmission path of the IPT systems. (a) Without misalignment. (b) With misalignment.

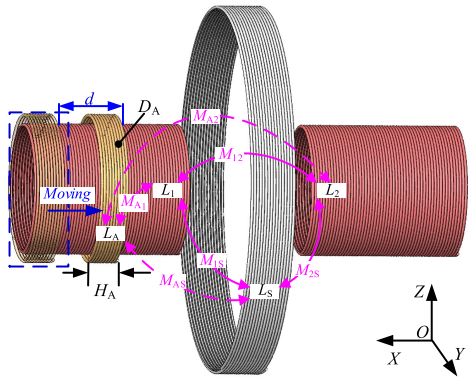

Fig. 5. Magnetic coupling structure with the novel auxiliary compensation coil.

III. Proposed Auxiliary Coil to Enhance Misalignment Tolerance

A. Auxiliary Coil Design and Analysis

In the actual wireless charging process for EBs, the charging voltage usually needs to be a constant standard dc voltage. Therefore, a voltage conversion topology is required to achieve CV characteristics. Although the magnetic coupling structure proposed in the previous Section II can greatly weaken the changes in mutual inductance caused by misalignment, the remaining mutual inductance changes will still cause significant changes in the wireless charging voltage. In order to eliminate voltage fluctuations caused by misalignment, an auxiliary compensation coil to further resist misalignment is proposed in this section, as shown in Fig. 5 yellow part. The effects of receiving coil misalignment can be eliminated by moving the coil position.

Since the transmitting coupler is designed as solenoid coils, to facilitate movement, the auxiliary coil is also designed as a solenoid. In addition, the short transmitting coils are not conducive to the placement and movement of the auxiliary coil. The auxiliary coil is attached to one side of the transmitting coils and its position can be adjusted to change the charging voltage. After adding the auxiliary coil, the structure of the magnetic coupler is shown in Fig. 5. In this configuration, L_A, L_1, L_2, and L_S are the self-inductances of the four coils, respectively. $M_{A1}, M_{A2}, M_{AS}, M_{12}, M_{1S}$, and M_{2S}, respectively, represent the mutual inductance between coils. The auxiliary coil self-inductance value L_A is much smaller than L_1, L_2, and is farther away from the transmitting coil on the other side. Therefore, M_{A2} can be considered negligible in circuit.

According to the inductance equivalent decoupling principle, the total self-inductance L_P and mutual inductance M_{AP}, M_{PS} of the transmitting coils can be expressed as

$$L_{\boldsymbol{P}} = L_1 + L_2 + 2M_{12} \tag{3}$$

$$\begin{cases} M_{AP} = M_{A1} \\ M_{PS} = M_{1S} + M_{2S}. \end{cases} \tag{4}$$

Therefore, the three mutual inductance parameters in the system are M_{AP}, M_{PS}, and M_{AS}. Among them, M_{PS} is only related to the relative position relationship between the transmitting coils and the receiving coil, and its value remains unchanged during the movement of the auxiliary coil. Besides, M_{AS} changes as the distance between the auxiliary coil and the receiving coil changes.

M_{AP} can be divided into three parts $M_{I\text{-}II}$, $M_{I\text{–}III}$, $M_{I\text{–}IV}$, as shown in Fig. 6. $M_{I\text{–}III}$ is the mutual inductance between the

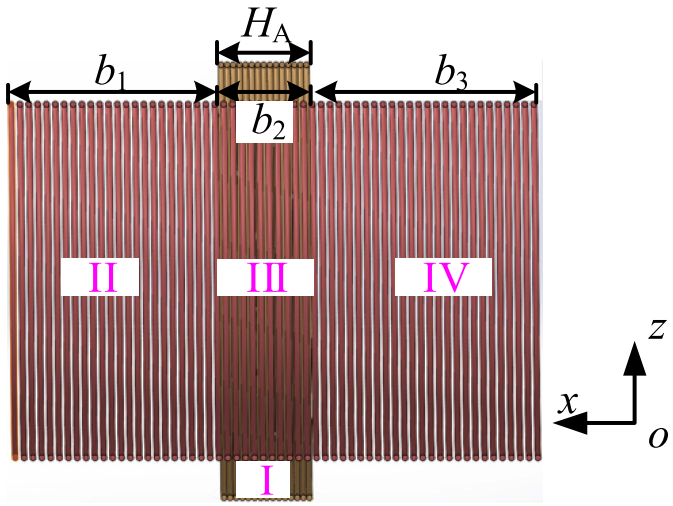

Fig. 6. Position relationship between the auxiliary coil and the transmitting coil.

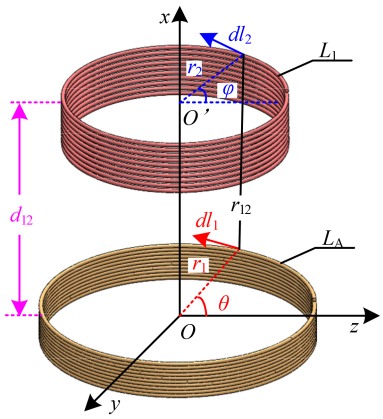

Fig. 7. Concentric coils in space coordinate system.

overlapping parts of the two coils in the *X*-direction. $M_{\text{I-II}}$ and $M_{\text{I–IV}}$ are the mutual inductance between two multiturn coils, and their center distances in the *X*-direction are $(b_1+b_2)/2$ and $(b_2+b_3)/2$, respectively. For $M_{\text{I-II}}$ and $M_{\text{I–IV}}$, [39] is referred and the solution process for $M_{\text{I-II}}$ is given as an example.

The specific analytical model is constructed based on the geometric configuration illustrated in Fig. 7. The *O-xyz* coordinate system is established with the geometric center of the auxiliary coil as the origin. *O* and *O*' are the geometric centers of the auxiliary coil L_A and the transmitting coil L_1 part II, and the geometric center of the transmitting coil part II is located on the *X*-axis. r_1 and r_2 are the radii of the two coils, d_{12} is the axial distance between the geometric centers of the two coils, dl_1 and dl_2 are the infinitesimals on the two coils, and r_{12} is the geometric distance between the two infinitesimals. The position of the auxiliary coil is fixed, and only the spatial relative position of the transmitting coil part II is changed for analysis. The geometric center coordinates of the transmitting coil part II are $(d_{12}, 0, 0)$.

When calculating the mutual inductance between any two single-turn coils, Neumann's formula is often used

$$M = \frac{\mu_0}{4\pi}\oint_{l_1}\oint_{l_2}\frac{d\vec{l_1}\cdot d\vec{l_2}}{r_{12}} \tag{5}$$

where μ_0 is the magnetic permeability of vacuum, In the *O-xyz* coordinate system, the coordinates of dl_1 are $(0, r_1\sin\theta, r_1\cos\theta)$, the coordinates of dl_2 are $(d_{12}, r_2\sin\varphi, r_2\cos\varphi)$, θ, $\varphi\in[0,2\pi]$. Substituting the above parameters into (5), the mutual inductance between single-turn circular coils can be obtained in this example. Since this structure can be regarded as a thin-walled solenoid, the mutual inductance between the single-turn coils is superimposed in the *X*-direction, and finally the $M_{\text{I-II}}$ expression is obtained

$$M_{\text{I–II}} = \frac{N_1N_2\mu_0r_1r_2}{4\pi}\int_0^{2\pi}\int_0^{2\pi} \times \frac{\cos(\theta-\varphi)}{\sqrt{r_1^2+r_2^2+d_{12}^2-2r_1r_2\cos(\theta-\varphi)}}d\theta d\varphi \tag{6}$$

where N_1, N_2 are the number of turns of the auxiliary coil L_A and the transmitting coil L_1 part II, respectively. Similarly, the mutual inductance calculation method of $M_{\text{I–IV}}$ can be obtained. When the auxiliary coil moves on the transmitting coil, the overlapping part of the two coils is always the length of the auxiliary coil, and the two coils have uniform turns and no magnetic core inside. $M_{\text{I–III}}$ remains unchanged during the movement. From (6), it can be analyzed that when d_{12} approaches 0, the mutual inductance changes rate increases sharply and the solution accuracy decreases. Therefore, this article uses the method of [40] to solve $M_{\text{I–III}}$ to improve the accuracy, and (7) can be obtained as follows:

$$M_{\text{I–III}} = \frac{b_2}{b_1+b_2+b_3}\times\frac{\mu_0\pi}{H_Ab_2\ln\left(\frac{r_1'}{r_1}\right)\ln\left(\frac{r_2'}{r_2}\right)} \times\int_0^{\infty}S(kr_{1'},kr_1)S(kr_{2'},kr_2)Q(kH_A,kb_2)dk \tag{7}$$

where r_1' and r_2' are the outer radii of the two coils after considering the thickness of the coil. After combining $M_{\text{I-II}}$, $M_{\text{I–III}}$, and $M_{\text{I–IV}}$, the expression of M_{AP} can be obtained

$$M_{\text{AP}} = M_{\text{I–II}} + M_{\text{I–III}} + M_{\text{I–IV}}. \tag{8}$$

In the process of reconstructing the auxiliary coil position, the change trends of M_{AP}, M_{PS}, and M_{AS} are shown in Fig. 8. As the auxiliary coil moves on the transmitting coil toward the receiving coil, *d* gradually increases. The mutual inductance M_{AP} first increases and then decreases. M_{AP} reaches a maximum value when moving to the center of the transmitting coil. Besides, M_{PS} remains constant throughout the process and is unaffected by the movement of the auxiliary coil. In addition, M_{AS} is small enough in the range of 0–80 mm relative to M_{AP} and the main mutual inductance M_{PS} of the wireless charging system power transfer. The relationship between the above parameters lays the foundation for ignoring the cross-inductance in the circuit model.

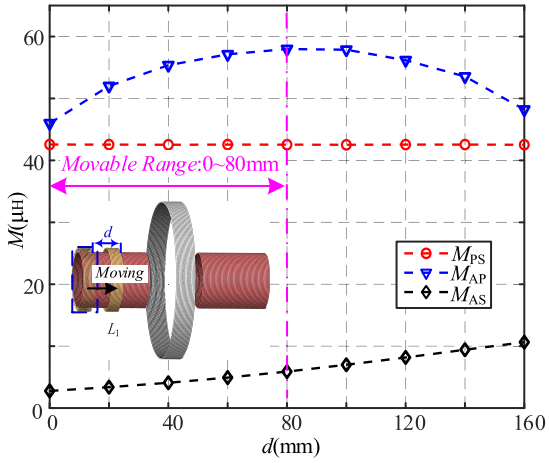

Fig. 8. Relationship curve between mutual inductance and the moving distance of the auxiliary coil.

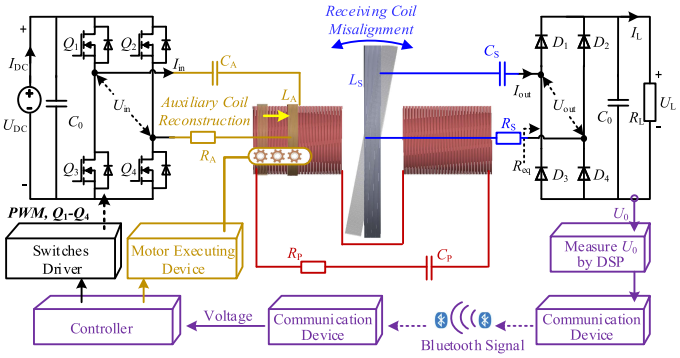

Fig. 9. Overall architecture of antimisalignment IPT system based on ACPR method.

B. Circuit Modeling and Analysis

The overall architecture of the antimisalignment IPT system is shown in Fig. 9. The circuit is mainly composed of dc power supply, load, full-bridge inverter circuit, rectifier circuit, magnetic coupling structure, and compensation capacitors. Among them, $U_{\rm dc}$ is the dc voltage source, $U_{\rm in}$ is the inverter output voltage, $U_{\rm out}$ is the rectifier input voltage, and $U_{\rm L}$ is the load voltage. Q_1–Q_4 are the MOSFETs of the full-bridge inverter, and D_1–D_4 are rectifier circuit diodes. $C_{\rm P}$, $C_{\rm S}$, $C_{\rm A}$ are the compensation capacitors for the coils and C_0 is the filter capacitor. $R_{\rm A}$, $R_{\rm P}$, $R_{\rm S}$ are the equivalent series resistance (ESR) of the circuits.

The power supply is connected to the auxiliary coil via an inverter, and the battery is ultimately charged through the receiving coil and rectifier. When misalignment occurs, the change in mutual inductance between the receiving coil and transmitting coils is reflected in the load voltage. The digital signal processing (DSP) with the sample module on the receiving side samples the receiving output voltage $U_{\rm L}$. When the voltage deviates from the standard charging voltage, the deviation signal is transmitted via the Bluetooth communication device on the receiving side to the communication device on the transmitting side. This signal drives the controller to drive the mechanical transmission device,

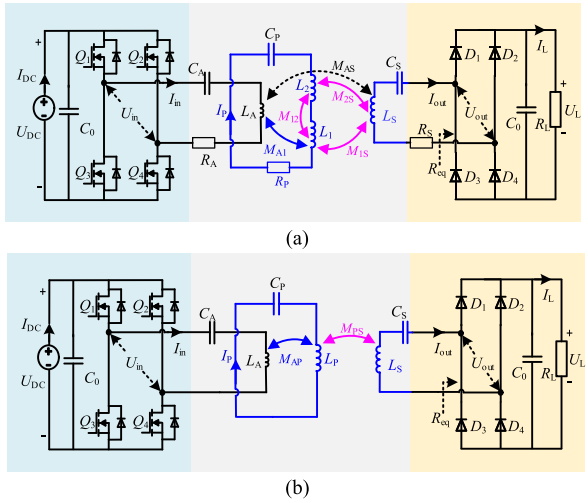

Fig. 10. Circuit model of IPT system incorporating auxiliary coil. (a) Circuit topology of the IPT system. (b) Simplified circuit topology.

and the position of the auxiliary coil is adjusted to achieve magnetic field reconstruction. Therefore, the change in mutual inductance can be compensated, and the impact of misalignment on IPT system parameters can be minimized. Under actual charging conditions, stable constant-voltage charging of EBs is achieved.

In order to better demonstrate the antimisalignment principle of this system, the circuit model incorporating the auxiliary coil for the IPT system is established in detail, as shown in Fig. 10(a). The ESR in the three *LC* series circuit is very low relative to the reactance value. Therefore, it can be negligible for the circuit characteristics analysis. According to formula (3) and formula (4), the transmitting coils L_1 and L_2 can be integrated as $L_{\rm P}$ with M_{12} considered as part of this overall self-inductance, and the mutual inductances $M_{1\rm S}$ and $M_{2\rm S}$ between the transmitting and receiving coils on both sides can also be considered as a whole $M_{\rm PS}$. Since $M_{\rm A2}$ is very small, the mutual inductance $M_{\rm AP}$ between the auxiliary coil and the transmitting coils can be regarded as $M_{\rm A1}$. Therefore, the circuit system in Fig. 10(a) can be described by the following equations:

$$\begin{cases} U_{\rm in} = \frac{1}{\mathbf{j}\omega \boldsymbol{C_A}} I_{\boldsymbol{in}} + \mathbf{j}\omega L_{\boldsymbol{A}} I_{\boldsymbol{in}} - \mathbf{j}\omega M_{\boldsymbol{AP}} I_{\boldsymbol{P}} - \mathbf{j}\omega M_{\boldsymbol{AS}} I_{\rm out} \\ \mathbf{j}\omega M_{\boldsymbol{AP}} I_{\boldsymbol{in}} = \frac{1}{\mathbf{j}\omega \boldsymbol{C_P}} I_{\boldsymbol{P}} + \mathbf{j}\omega L_{\boldsymbol{P}} I_{\boldsymbol{P}} - \mathbf{j}\omega M_{\boldsymbol{PS}} I_{\boldsymbol{out}} \\ \mathbf{j}\omega M_{\boldsymbol{PS}} I_{\boldsymbol{P}} = \frac{1}{\mathbf{j}\omega \boldsymbol{C_S}} I_{\boldsymbol{out}} + \mathbf{j}\omega L_{\boldsymbol{S}} I_{\rm out} - \mathbf{j}\omega M_{\boldsymbol{AS}} I_{\rm in} + \mathbf{R_{eq}} I_{\boldsymbol{out}}. \end{cases} \tag{9}$$

Since the auxiliary coil has a small self-inductance and its moving range is relatively far away from the receiving coil, the corresponding coupling coefficient is relatively weak. In Fig. 8, $M_{\rm AS}$ is several times much lower than $M_{\rm AP}$ and $M_{\rm PS}$ during the auxiliary coil moving. In order to facilitate the analysis of the output characteristics of the system, $M_{\rm AS}$ can be neglected. Based on the circuit model Fig. 10(a) simplified from Fig. 9, the simplified circuit can be further obtained, as shown in Fig. 10(b), with the ignorance of $M_{\rm AS}$. Under this condition, the ideal ac circuit of the IPT system under this condition is shown in Fig. 11.

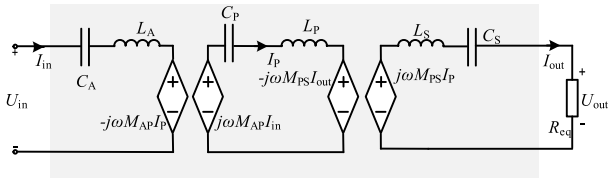

Fig. 11. Ideal AC circuit of the IPT system.

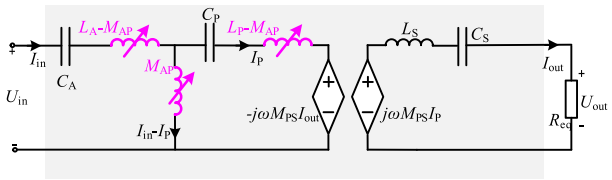

Fig. 12. IPT system based on equivalent T/S compensation topology.

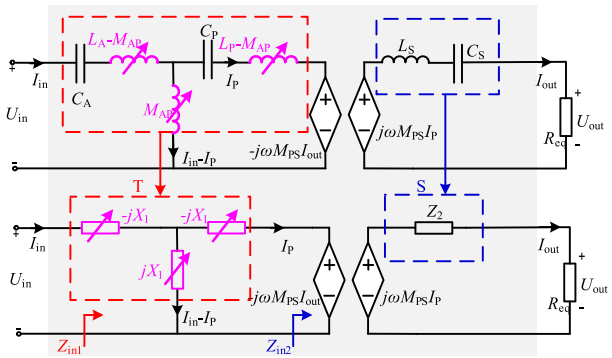

Fig. 13. Circuit model after resonant transformation.

Based on above simplified process, (9) can be transformed as

$$\begin{cases} U_{\text{in}} = \frac{1}{\mathbf{j}\omega \mathbf{C}_{\boldsymbol{A}}} I_{\boldsymbol{in}} + \mathbf{j}\omega(L_{\boldsymbol{A}} - M_{\boldsymbol{AP}}) I_{\boldsymbol{in}} + \mathbf{j}\omega M_{\boldsymbol{AP}}(I_{\boldsymbol{in}} - I_{\boldsymbol{P}}) \\ \mathbf{j}\omega M_{\boldsymbol{AP}}(I_{\boldsymbol{in}} - I_{\boldsymbol{P}}) = \frac{1}{\mathbf{j}\omega \mathbf{C}_{\boldsymbol{P}}} I_{\boldsymbol{P}} + \mathbf{j}\omega(L_{\boldsymbol{P}} - M_{\boldsymbol{AP}}) I_{\boldsymbol{P}} \\ \qquad\qquad - \mathbf{j}\omega M_{\boldsymbol{PS}} I_{\boldsymbol{out}} \\ \mathbf{j}\omega M_{\boldsymbol{PS}} I_{\boldsymbol{P}} = \frac{1}{\mathbf{j}\omega \mathbf{C}_{\boldsymbol{S}}} I_{\boldsymbol{out}} + \mathbf{j}\omega L_{\boldsymbol{S}} I_{\boldsymbol{out}} + \mathbf{R}_{\boldsymbol{eq}} I_{\boldsymbol{out}}. \end{cases} \tag{10}$$

According to (10), the circuit structure shown in Fig. 12 can be obtained. It can be found the circuit is an IPT system with equivalent T/S compensation, consisting of a T circuit and an *LC* series circuit. In order to reduce reactive power and improve power transfer efficiency, the circuit is designed to operate under a resonance state, as shown in Fig. 13. When the circuit is resonant, the following formula can be applied:

$$\omega L_{\text{i}} - \frac{1}{\omega C_{\text{i}}} = 0, \text{i} = A, P, S. \tag{11}$$

According to the resonance conditions of the T-type network and the *LC* series network, the circuit parameters can be expressed as

$$\mathbf{Z_2} = j\boldsymbol{\omega}\mathbf{L_S} - j\frac{1}{\boldsymbol{\omega}\mathbf{C_S}} = 0 \tag{12}$$

$$\begin{aligned} \mathbf{X_1} &= \frac{1}{\boldsymbol{\omega}\mathbf{C_A}} - \boldsymbol{\omega}(\mathbf{L_A} - \mathbf{M_{AP}}) \\ &= \frac{1}{\boldsymbol{\omega}\mathbf{C_P}} - \boldsymbol{\omega}(\mathbf{L_P} - \mathbf{M_{AP}}) = \boldsymbol{\omega}\mathbf{M_{AP}}. \end{aligned} \tag{13}$$

When the resonance condition is met, all reactance in the system is offset, and the parameters of the circuit system can be described as

$$\mathbf{Z_{in1}} = \frac{M_{\boldsymbol{AP}}^2 \mathbf{R}_{\text{eq}}}{M_{\boldsymbol{PS}}^2}, \mathbf{Z_{in2}} = \frac{\omega^2 M_{\boldsymbol{PS}}^2}{\mathbf{R}_{\text{eq}}} \tag{14}$$

$$\mathbf{I_P} = -\frac{\mathbf{U_{in}}}{\mathbf{j}\omega\mathbf{M_{AP}}}, \quad \mathbf{I_{in}} = \frac{\mathbf{U_{in}} M_{\boldsymbol{PS}}^2}{M_{\boldsymbol{AP}}^2 \mathbf{R}_{\text{eq}}} \tag{15}$$

$$\mathbf{U_{out}} = -\frac{\mathbf{M_{PS}}}{\mathbf{M_{AP}}} \mathbf{U}_{\text{in}}. \tag{16}$$

Among them, Z_{in1} and Z_{in2} are the input impedance of each stage, respectively. I_{in} and I_{P} are the currents flowing through the circuit, and U_{out} is the ac side output voltage. Given that the position of the auxiliary coil is fixed, U_{out} only depends on U_{in}. The voltage transformation ratio g can be expressed as

$$g = \left| \frac{\mathbf{U}_{\text{out}}}{\mathbf{U}_{\text{in}}} \right| = \frac{\mathbf{M_{PS}}}{\mathbf{M_{AP}}}. \tag{17}$$

In Figs. 12 and 13, the mutual inductance M_{AP} is a variable inductance marked in magenta in the circuit, and its value can be changed by moving the position of the auxiliary coil. The diagonal arrows next to the parameters with M_{AP} items indicate that the mutual inductance is adjustable [41]. Therefore, the resonant network parameters can be reconstructed and the voltage transformation ratio can be adjusted by changing M_{AP}.

In the process of adjusting the position of the auxiliary coil, maintaining the consistency of the change degree of M_{AP} and M_{PS} is particularly critical to the system's ability to maintain stable charging capability even under misalignment conditions. In addition, M_{AS} is small enough in the range of 0–80 mm relative to M_{AP} and the main mutual inductance M_{PS} of the charging system energy transmission according to the black curve in Fig. 8. Therefore, the auxiliary coil compensation range can be selected from 0 to 80 mm. Thus, the impact of M_{AS} can be minimized and the feasibility of (16) is ensured in practical applications. Besides, M_{AP} decreases almost symmetrically on both sides, and a sufficient voltage ratio can be obtained in the range of 0–80 mm.

It should be emphasized that when the auxiliary coil moves within the specified range, the change in mutual inductance in the system is M_{AP}. When the coils are misaligned, the change in mutual inductance in the system is M_{PS}. Although the mutual inductance between the transmission coils varies due to their positional relationship, the corresponding self-inductances L_{A}, L_{P}, and L_{S} of the coils remain unchanged during operation because of the unchanged magnetic circuit. Since the capacitors C_{A}, C_{P}, and C_{S} compensate for the corresponding self-inductances, the charging system's resonance is maintained.

In summary, combining the contents of *Chapter II* and *Section A* and *Section B* of *Chapter III*, the overall design process of the magnetic coupler in this article is shown in Fig. 14.

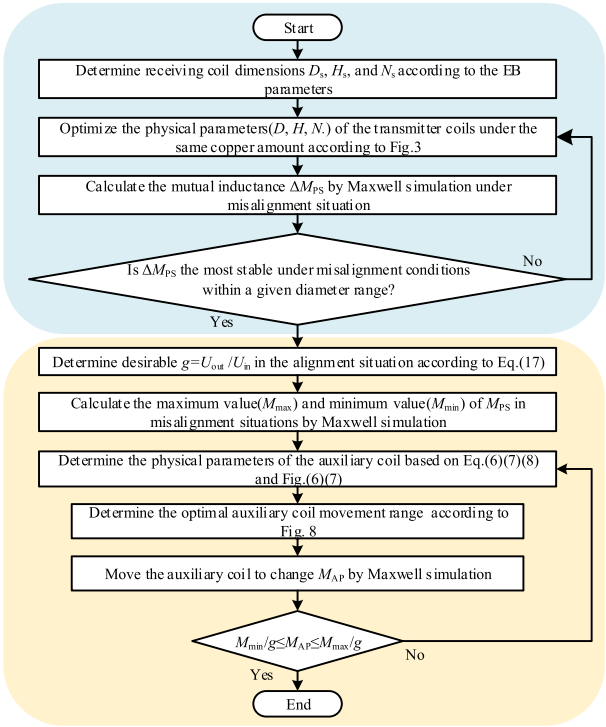

Fig. 14. Design flow of the proposed magnetic coupler for EBs wireless charging.

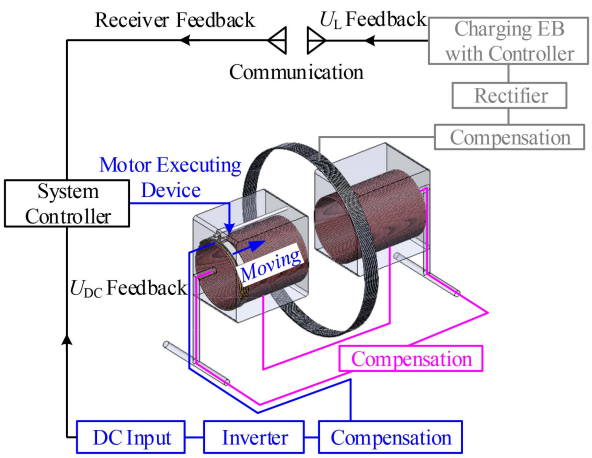

Fig. 15. Diagram of the proposed ACPR method for anti-misalignment EBs wireless charging system.

C. Auxiliary Coil Position Reconstruction Method for Antimisalignment

Based on the abovementioned analysis and design, a novel ACPR method is proposed to improve the misalignment tolerance of wireless charging systems. The antimisalignment adjustment scheme is shown in Fig. 15. The charging voltage of the electric bicycle under misalignment is corrected by reconstructing the position of the auxiliary coil. The key advantages of the proposed method are its high accuracy against misalignment and the simplicity of the control strategy.

The working principle of the proposed method is explained as follows. The wireless charging voltage at the receiver is monitored during the charging process. Then, the measured charging voltage is compared with the EB's preset rated charging voltage to assess the degree of performance degradation caused by misalignment. The detected voltage deviation is transmitted to the transmitter through a communication module and the executing device is activated for motor transmission by the controller. The spatial position of the auxiliary coil is dynamically adjusted along the axial direction, effectively resetting the mutual inductance parameters between the power transmission coils to compensate for alignment errors. Through this active regulation mechanism, the charging voltage is stabilized and power transfer efficiency is restored, allowing the receiver to continue operating near its optimal performance point even in the event of coil misalignment.

In summary, a wireless charging system consisting of two cylindrical transmission coils on both sides with an auxiliary coil nested within one side of the transmission coils is proposed in this article, and it demonstrates strong antimisalignment performance in three dimensions: X, Y, and angular. A method for achieving active antimisalignment by adjusting the position of the auxiliary coil to reconfigure the circuit topology is the key in this article. In the field of wireless charging, this method breaks the limitation of traditional charging solutions that rely on optimizing the magnetic structure or circuit topology to achieve passive antimisalignment. At the same time, the simple single closed-loop control strategy of this solution is more stable and easier to maintain in actual use compared to other complex control strategies. The proposed misalignment tolerance improvement method provides a flexible solution to the problem of poor charging capacity caused by complex parking situations of electric bicycles in actual scenarios. Table I compares the differences between this article and common misalignment tolerance solutions to highlight the uniqueness of this article. Among them, general methods coil design, compensation topology, and control strategy in the field of misalignment tolerance are included.

IV. Prototype Construction and Experimental Results

An experimental prototype is built to verify the misalignment tolerance capability of the proposed magnetic coupling structure and ACPR method in Fig. 16. The system architecture and parameters correspond to the descriptions in Figs. 9 and 10. The prototype system is mainly composed of dc power supply ITECH IT6723H, auxiliary power supply RIGOL DP823, primary circuit, secondary circuit, magnetic coupling structure, compensation network, DSP, motor executing device, electronic load ITECH IT8512A, and oscilloscope KEYSIGHT DSOX4024G. The parameters of the experimental prototype system are shown in Table II.

According to the standard charging voltage of EBs, the input voltage is selected to be 72 V, and the ideal output voltage is 60 V. Misalignment in all three dimensions is taken into account, including Y, X, and rotation angles. Therefore, $\Delta y =$ 0–160 mm, $\Delta x = -20$–20 mm and rotation angle misalignment

TABLE I
COMPARISON OF DIFFERENT METHODS ABOUT ANTIMISALIGNMENT

Reference	Antimisalignment Method	Implementation Principle	Control Complexity	Design Flexibility	Anti-Misalignment Properties
This work	Novel ACPR Method	Circuit Topology Reconfiguration	Low	High	Active
[42]	Coil Design	Complement of Mutual Inductance	-	Moderate	Passive
[43]		Editable Magnetic Field	High	Moderate	Active
[44]		Optimization Algorithm	-	High	Passive
[45]	Compensation Topology	Novel Topology	Low	Moderate	Passive
[36]		Parameter Characteristics	-	High	Passive
[46]	Control Strategy	Switch Array Adjustment	High	High	Active
[47]		Multiloop Dynamic Tuning	High	Low	Active

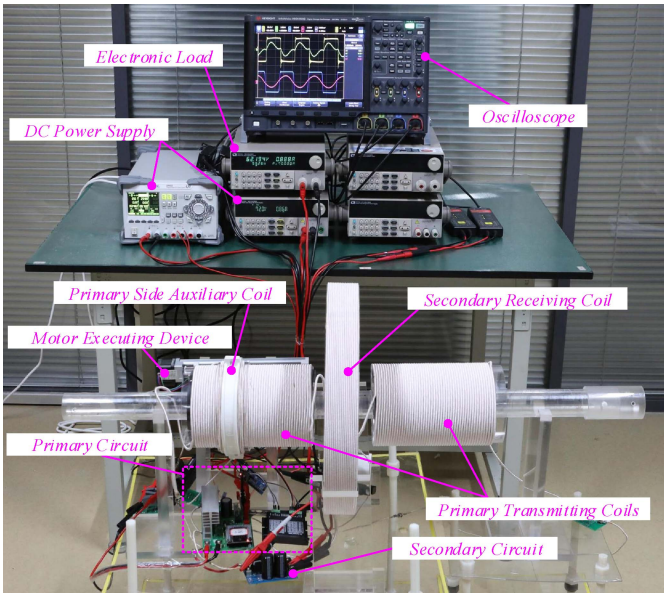

Fig. 16. Experimental prototype.

TABLE II
MAIN PARAMETERS OF THE PROTOTYPE

Parameter	Value/Type	Parameter	Value/Type
f_0	150 kHz	C_A	26.05 nF
$Q_1 - Q_4$	IRFBA22N50	**Alignment Situation, Δy = 0 mm**	
$D_1 - D_4$	MBR40200WT	d	66 mm
L_1	186.11 μH	M_{1S}	22.01 μH
L_2	185.23 μH	M_{2S}	25.50 μH
R_P	450.58 mΩ	M_{PS}	47.51 μH
M_{12}	8.33 μH	M_{AP}	53.86 μH
L_P	388.00 μH	**Misalignment Situation, Δy = 160 mm**	
C_P	2.90 nF	d	52 mm
L_S	240.90 μH	M_{1S}	19.85 μH
R_S	599.99 mΩ	M_{2S}	22.13 μH
C_S	4.68 nF	M_{PS}	41.98 μH
L_A	43.53 μH	M_{AP}	48.87 μH
R_A	250.12 mΩ		

$\Delta\alpha = -18°$–$18°$ are used as the misalignment situation for the efficiency experiment.

The efficiency variation against different misalignment positions (in Y, X, and α directions) and loads is illustrated in Fig. 17. It can be seen that the efficiency can always be maintained at a high level, and the minimum efficiency is about 86%, which indicates the high-efficiency characteristics of this system. Among them, under the same load resistance, the misalignment process will not cause drastic fluctuations in system efficiency.

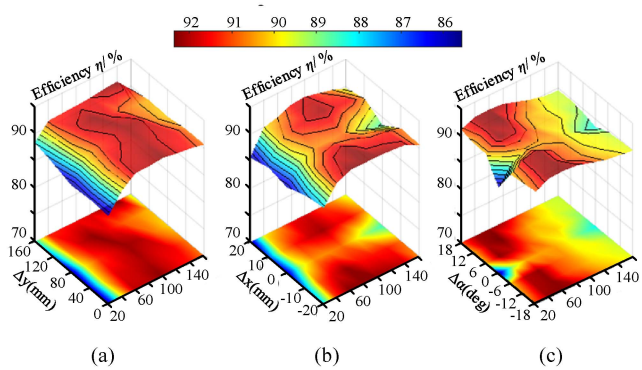

Fig. 17. Impact of misalignment distance and R_L on system efficiency. (a) Y-direction. (b) X-direction. (c) Angular direction.

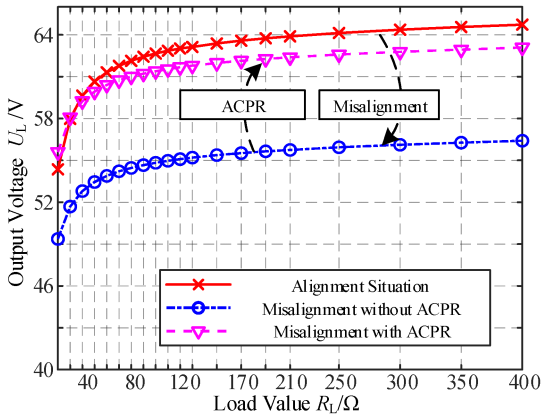

Fig. 18. Output voltage curves of the IPT system with alignment, $\Delta y = 160$ mm misalignment and ACPR method.

Based on the abovementioned experiment, the system voltage-power-efficiency characteristics and the ACPR method under a large misalignment are verified in Figs. 18 and 19. Since the impact of misalignment is the most significant in Y-direction among the three situations, as shown in Fig. 3(a)–(c), the following experimental analysis only depicts the changes under $\Delta y = 160$ mm dimension to make the experimental results more intuitive.

The output voltage characteristic curves of the system in three situations are obtained, as shown in Fig. 18. The experimental

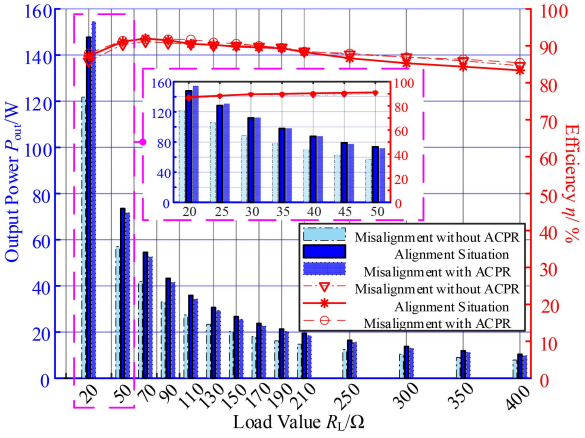

Fig. 19. Output power and efficiency of the IPT system under different situations.

results of the output voltage in the alignment situation, misalignment without ACPR method and misalignment with ACPR method are represented by the red, blue, and magenta curves in the figure, respectively.

The proposed ACPR method is significantly validated by the trends of the curves. As the common trend of the three curves, when the load resistance value is low, the fluctuation trend of the output voltage with load changes is more obvious. When the load resistance value increases to a certain extent, the output voltage approximately exhibits the characteristics of a CV source. First, when the receiving coil is aligned, the voltage change trend is shown in the red curve. In addition, the output voltage in the misalignment situation without ACPR method is significantly reduced compared to the alignment situation, as shown in the blue curve. After this, the position of the auxiliary coil is reconstructed and the voltage drop is compensated. At this time, the impact of misalignment on the output voltage can be almost eliminated by adjusting the position of the auxiliary compensation coil, as shown in the magenta curve.

The efficiency and power graphs for alignment, misalignment, and ACPR method are completed synchronously, as shown in Fig. 19. The changing trend of efficiency is represented by a dotted curve, and the output power is represented by a histogram. Power and efficiency are distinguished in this figure by blue and red, corresponding to the left and right vertical axes, respectively. According to the trend of the above experimental results, the output power of the system will be reduced in the misalignment situation. Compensating by moving the auxiliary coil eliminates the effect of misalignment on power. The system efficiency under the three conditions of alignment, misalignment and ACPR method fluctuates slightly. The voltage drops caused by misalignment will cause a sudden drop in output power. However, under the ACPR method, the system power is also restored. In addition, the system efficiency remains above 90% in a wide range, and when the load is 70 Ω, the maximum system efficiency reaches 91.18%.

The power loss distribution of the IPT system at the maximum efficiency point is shown in Fig. 20. The losses of the proposed IPT system are divided into the following parts [48],

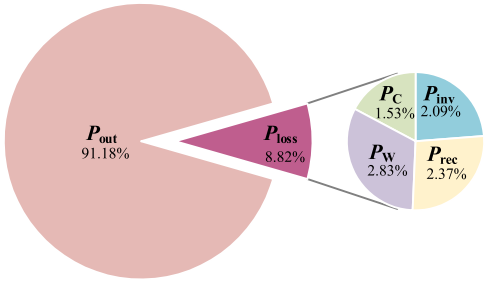

Fig. 20. Power loss distribution of the IPT system.

[49]. Rectifier circuit losses $P_{\rm rec}$, inverter circuit losses $P_{\rm inv}$, and equivalent resistance losses $P_{\rm Cu}$ in the system. Rectifier circuit losses $P_{\rm rec}$ and inverter circuit losses $P_{\rm inv}$ are caused by uncontrolled diodes and MOSFET switches, respectively. Based on the rectifier and inverter device models, $P_{\rm rec}$ and $P_{\rm inv}$ can be calculated as follows:

$$P_{\rm rec} = 2\left(\frac{2\sqrt{2}}{\pi}U_{\rm Dio}I_{\rm out} + R_{\rm Dio}I_{\rm out}^2\right) \tag{18}$$

$$P_{\rm inv} = 2R_{\rm MOS}I_{\rm in}^2. \tag{19}$$

Among them, $R_{\rm Dio}$ and $R_{\rm MOS}$ are the ON-resistance of the rectifier diode and MOSFET, respectively, and $U_{\rm Dio}$ is the forward conduction voltage drop of the rectifier diode.

The copper loss $P_{\rm Cu}$ of this IPT system includes two parts, one is the loss $P_{\rm W}$ caused by the wire ESR, and the other is the loss $P_{\rm C}$ generated on the capacitor

$$P_{\rm W} = I_{\rm in}^2R_{\rm WA} + I_{\rm P}^2R_{\rm WP} + I_{\rm out}^2R_{\rm WS} \tag{20}$$

$$P_{\rm C} = I_{\rm in}^2R_{\rm CA} + I_{\rm P}^2R_{\rm CP} + I_{\rm out}^2R_{\rm CS} \tag{21}$$

where $R_{\rm WA}$, $R_{\rm WP}$, and $R_{\rm WS}$ are the sum of the ESR in the auxiliary coil, transmitting coils, and receiving coil loops, respectively. $R_{\rm CA}$, $R_{\rm CP}$, $R_{\rm CS}$ are the equivalent resistance of the capacitors in the corresponding loops, respectively.

Therefore, the components and proportions of $P_{\rm loss}$ are as follows. Rectifier loss $P_{\rm rec}$ and inverter loss $P_{\rm inv}$ account for 2.37% and 2.09%, respectively, the equivalent resistance loss $P_{\rm W}$ of the circuit accounts for 2.83%, and the equivalent resistance loss $P_{\rm C}$ of the compensation capacitor accounts for 1.53%. Thus, the wireless power transfer with high efficiency is achieved.

The ac and dc waveforms of the magnetic coupler in alignment when the load is 50 Ω, 70 Ω, and 130 Ω are shown in Fig. 21. It can be seen that the phase of $U_{\rm in}$ is slightly ahead of $I_{\rm in}$, the phases of the fundamental wave components are basically consistent. The zero phase angle input is realized, and the resonance state is reached. In addition, the ac current waveform will be distorted by the equivalent T/S/compensation topology. Due to the influence of harmonics, the waveform of the input dc current in Fig. 21(b), (d), and (f) has certain fluctuations.

The dynamic response process of the output voltage and current of this IPT system under the load of 70 Ω is visually displayed in Fig. 22. The output voltage drops from 61.51 V to 53.30 V because of misalignment. The deviation between the output voltage and the rated output voltage is detected in

TABLE III
COMPARISON WITH SIMILAR WORKS IN RECENT YEARS

Reference	This Work	[14]	[15]	[16]	[18]
Anti-Misalignment Method	ACPR Method	Magnetic Structure	Control Strategy	No	No
Dc–dc Efficiency	91.18%	90.0%	94%	86.0%	91.9%
Receiving Coil Position	Hollow Frame of EB	Bicycle Kickstands	-	Bicycle Frame	Bicycle Wheel Spoke
Ferrite Core	No	Yes	Yes	Yes	Yes
Compensation Topology	Equivalent T/S	-	S-S	S-S	S-LCC
Power	147.69 W	200 W	96 W	400 W	175.5 W
Input Voltage/ Output Voltage	72V/60 V	40 V	9–27 V/48 V	110 V/48 V,72 V	42 V
Antimisalignment Capabilities	*X*-axis: ± 20 mm *Y*-axis: ± 160 mm α: ± 180° With 86% efficiency	*X*-axis: ± 20 mm *Y*-axis: ± 20 mm With 89% efficiency	*Z*-axis: ± 300 mm With 70% efficiency	-	-

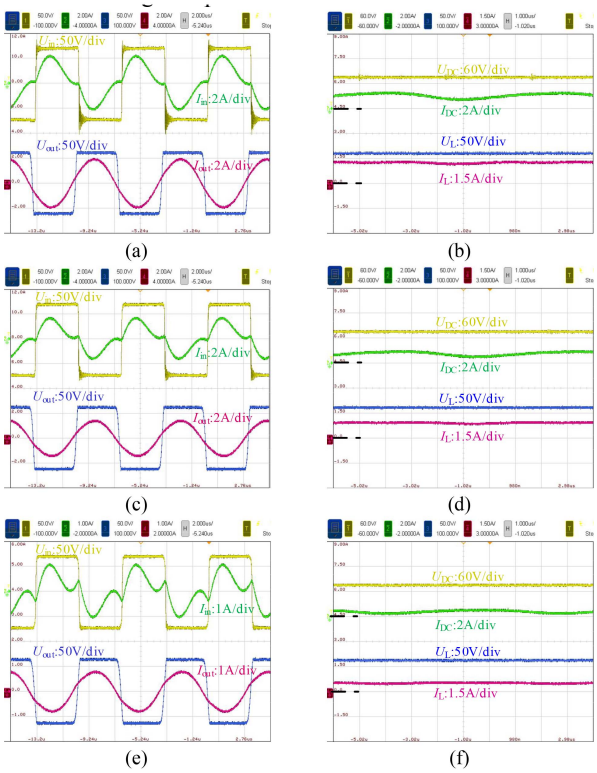

Fig. 21. Waveform of IPT system under alignment conditions. (a) AC waveform when $U_{dc} = 72$ V, $R_L = 50\ \Omega$. (b) DC waveform when $U_{dc} = 72$ V, $R_L = 50\ \Omega$. (c) AC waveform when $U_{dc} = 72$ V, $R_L = 70\ \Omega$. (d) DC waveform when $U_{dc} = 72$ V, $R_L = 70\ \Omega$. (e) AC waveform when $U_{dc} = 72$ V, $R_L = 130\ \Omega$. (f) DC waveform when $U_{dc} = 72$ V, $R_L = 130\ \Omega$.

misalignment situation, and the motor is driven by the deviation signal to change the spatial position of the auxiliary coil to reconstruct the system parameters. The output voltage rises back to 60.45 V and the voltage inaccuracy caused by the misalignment can be completely eliminated.

Furthermore, Table III is a comparison of the high misalignment-tolerant EBs wireless charging system based on the auxiliary coil position-reconfigurable resonant network and other typical EBs wireless charging systems in recent years. Compared with the work in [15], [16], and [18], the system in this article exhibits higher misalignment tolerance in multiple directions, lower system design complexity, and a simple control

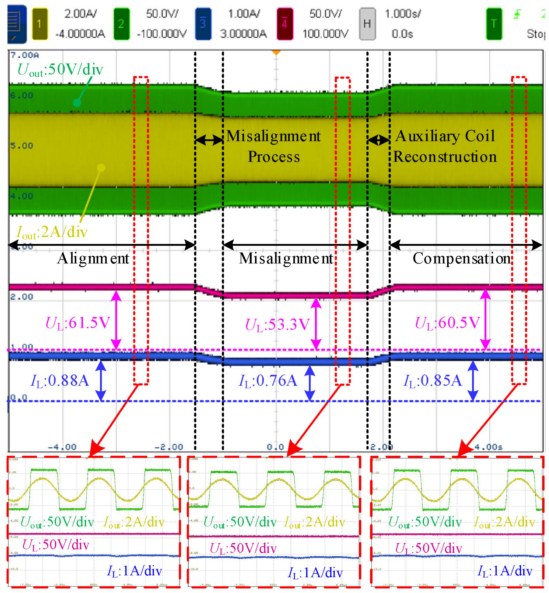

Fig. 22. Dynamic response waveform of proposed IPT system when $U_{dc} = 72$ V, $R_L = 70\ \Omega$.

scheme, demonstrating obvious advantages in the field of EBs charging. Compared with the work in [14], [15], [16], and [18], only four solenoid coils are used in this article, without additional ferrite cores, thus reducing both the weight and cost of the system. The solution of wireless charging through the hollow frame of electric bicycle is proposed by the system of this article. In addition, the proposed novel auxiliary compensation coil to improve the constant voltage charging capability of EBs is proposed for the first time, and the purpose of antimisalignment is achieved by changing the system resonance network parameters. In summary, the work proposed in this article has strong engineering practicability and application prospects.

V. CONCLUSION

A wireless charging system architecture composed of a receiving coil assembled in the hollow frame of electric bicycle and a transmitting coil integrated into the parking bracket is proposed in this article. The proposed magnetic coupling structure has misalignment tolerance in three dimensions including axial,

longitudinal, and angular directions. Misalignment tolerance is further improved by optimizing the parameters of the cylindrical solenoid transmitting coil. A novel auxiliary compensation coil is embedded on the transmitting coils. The auxiliary compensation coil, transmitting coils, and receiving coil are compensated by series capacitance. The circuit model of the system is built, analyzed, simplified, and transformed. An equivalent T/S resonant network with constant voltage output characteristics is obtained. By adjusting the position of the auxiliary coil with a motor executing device, the change in mutual inductance between the transmitting and receiving coil can be counteracted after the receiving coil is misaligned. The voltage transformation ratio regains the expected target through the reconstructed resonant network parameters by the ACPR method. A prototype platform simulating wireless charging for EBs is built. The system's strong anti-misalignment capability is verified, and its efficiency is consistently maintained a high level around 90%.

REFERENCES

[1] S. Jayalath and A. Khan, "Design, challenges, and trends of inductive power transfer couplers for electric vehicles: A review," *IEEE J. Emerg. Sel. Topics Power Electron.*, vol. 9, no. 5, pp. 6196–6218, Oct. 2021.

[2] Y. Wang, Z. Sun, Y. Guan, and D. Xu, "Overview of megahertz wireless power transfer," *Proc. IEEE*, vol. 111, no. 5, pp. 528–554, May 2023.

[3] E. S. Lee, D. Kim, and S. Y. Jeong, "Triangular DQ Tx coils of wireless EV chargers for large misalignment tolerances," *IEEE Trans. Veh. Technol.*, vol. 72, no. 11, pp. 14179–14188, Nov. 2023.

[4] A. Mostafa, Y. Wang, S. Tangirala, H. Zhang, and F. Lu, "A 5 kW hull-compatible inductive charging system with 360° folded spatial unipolar coupler for autonomous underwater vehicles (AUVs)," *IEEE Trans. Ind. Appl.*, vol. 59, no. 6, pp. 7001–7012, Nov./Dec. 2023.

[5] S. Wu, C. Cai, H. Zhang, X. Liu, and W. Chai, "A free-positioning IPT system via reconfigurable coil array transmitter for unmanned aerial vehicle applications," *IEEE Trans. Transp. Electrific.*, vol. 10, no. 4, pp. 8746–8757, Dec. 2024.

[6] J. Yin, S. Mekhilef, P. Darvish, H. Mokhlis, and T. K. Soon, "A new cross-overlapped decoupling coil structure for EV dynamic inductive wireless charging system," *IEEE Trans. Ind. Electron.*, vol. 72, no. 2, pp. 1314–1324, Feb. 2025.

[7] P. Gu, D. Yang, G. Li, B. Zhou, F. Wei, and H. Guan, "Analysis and design of discrete ferrite rings to improve the efficiency of meter-range wireless gap inductive power transfer system," *IEEE Trans. Power Electron.*, vol. 38, no. 10, pp. 11802–11813, Oct. 2023.

[8] P. Gu et al., "A 2.5m long-range IPT system based on Domino cylindrical solenoid coupler compensated respectively in layers," *IEEE Trans. Ind. Electron.*, vol. 70, no. 2, pp. 1409–1420, Feb. 2023.

[9] P. Gu et al., "Reconfigurable inductive power transfer scheme across reinforced concrete walls for building attached photovoltaic grid connection," *IEEE Trans. Power Electron.*, vol. 40, no. 10, pp. 15891–15904, Oct. 2025.

[10] Y. Zhang, S. Chen, X. Li, and Y. Tang, "Design methodology of free-positioning nonoverlapping wireless charging for consumer electronics based on antiparallel windings," *IEEE Trans. Ind. Electron.*, vol. 69, no. 1, pp. 825–834, Jan. 2022.

[11] C. Cai et al., "Hybrid interference field mitigation of dual-rectangular transmitter pad for universal wireless charging area expansion," *IEEE Trans. Transp. Electrific.*, vol. 10, no. 2, pp. 3816–3827, Jun. 2024.

[12] C. Jiang, D. E. Gaona, Y. Shen, H. Zhao, K. T. Chau, and T. Long, "Low-frequency medium power capacitor-free self-resonant wireless power transfer," *IEEE Trans. Ind. Electron.*, vol. 68, no. 11, pp. 10521–10533, Nov. 2021.

[13] L. Li et al., "Investigation and numerical reconstruction of a full-scale electric bicycle fire experiment in high-rise residential building," *Case Stud. Thermal Eng.*, vol. 37, pp. 12304, Sep. 2022.

[14] H. Z. Z. Beh, G. A. Covic, and J. T. Boys, "Investigation of magnetic couplers in bicycle kickstands for wireless charging of electric bicycles," *IEEE J. Emerg. Sel. Topics Power Electron.*, vol. 3, no. 1, pp. 87–100, Mar. 2015.

[15] P. K. Joseph, D. Elangovan, and P. Sanjeevikumar, "System architecture, design, and optimization of a flexible wireless charger for renewable energy-powered electric bicycles," *IEEE Syst. J.*, vol. 15, no. 2, pp. 2696–2707, Jun. 2021.

[16] H. Z. Z. Beh, G. A. Covic, and J. T. Boys, "Wireless fleet charging system for electric bicycles," *IEEE J. Emerg. Sel. Topics Power Electron.*, vol. 3, no. 1, pp. 75–86, Mar. 2015.

[17] Y. Li, J. Hu, F. Chen, S. Liu, Z. Yan, and Z. He, "A new-variable-coil-structure-based IPT system with load-independent constant output current or voltage for charging electric bicycles," *IEEE Trans. Power Electron.*, vol. 33, no. 10, pp. 8226–8230, Oct. 2018.

[18] Y. Chen, Z. Kou, Y. Zhang, Z. He, R. Mai, and G. Cao, "Hybrid topology with configurable charge current and charge voltage output-based WPT charger for massive electric bicycles," *IEEE J. Emerg. Sel. Topics Power Electron.*, vol. 6, no. 3, pp. 1581–1594, Sep. 2018.

[19] A. Triviño-Cabrera, J. M. González-González, and J. A. Aguado, "Design and implementation of a cost-effective wireless charger for an electric bicycle," *IEEE Access*, vol. 9, pp. 85277–85288, 2021.

[20] R. Mai, Y. Chen, Y. Li, Y. Zhang, G. Cao, and Z. He, "Inductive power transfer for massive electric bicycles charging based on hybrid topology switching with a single inverter," *IEEE Trans. Power Electron.*, vol. 32, no. 8, pp. 5897–5906, Aug. 2017.

[21] E. G. Marques, V. S. Costa, M. S. Perdigão, and A. M. S. Mendes, "Double coupling In-wheel IPT system for electric vehicles," *IEEE Trans. Veh. Technol.*, vol. 72, no. 10, pp. 12757–12769, Oct. 2023.

[22] H. Wang, K. W. E. Cheng, and Y. Yang, "A new resonator design for wireless battery charging systems of electric bicycles," *IEEE J. Emerg. Sel. Topics Power Electron.*, vol. 10, no. 5, pp. 6009–6019, Oct. 2022.

[23] X. Duan, G. Yan, J. Huang, J. Qiu, C. Rong, and W. Han, "A single-input dual-output wireless power and information transfer system using DDQ nested coils for motor drives," *IEEE J. Emerg. Sel. Topics Power Electron.*, to be published, doi: 10.1109/JESTPE.2025.3565497.

[24] B. Zhang, J. Chen, X. Wang, W. Xu, C. Lu, and Y. Lu, "High-power-density wireless power transfer system for autonomous underwater vehicle based on a variable ring-shaped magnetic coupler," *IEEE Trans. Transp. Electrific.*, vol. 10, no. 2, pp. 3061–3074, Jun. 2024.

[25] Q. Zhu, Y. Zhang, C. Liao, Y. Guo, L. Wang, and F. Li, "Experimental study on asymmetric wireless power transfer system for electric vehicle considering ferrous chassis," *IEEE Trans. Transp. Electrific.*, vol. 3, no. 2, pp. 427–433, Jun. 2017.

[26] J. Li, F. Yin, and L. Wang, "Transmission efficiency of different shielding structures in wireless power transfer systems for electric vehicles," *CSEE J. Power Energy Syst.*, vol. 7, no. 6, pp. 1247–1255, Nov. 2021.

[27] V.-B. Vu et al., "Operation of inductive charging systems under misalignment conditions: A review for electric vehicles," *IEEE Trans. Transp. Electrific.*, vol. 9, no. 1, pp. 1857–1887, Mar. 2023.

[28] W. Pan, C. Liu, H. Tang, Y. Zhuang, and Y. Zhang, "An interoperable electric vehicle wireless charging system based on mutually spliced double-D coil," *IEEE Trans. Power Electron.*, vol. 39, no. 3, pp. 3864–3872, Mar. 2024.

[29] Y. Yao, S. Gao, Y. Wang, X. Liu, X. Zhang, and D. Xu, "Design and optimization of an electric vehicle wireless charging system using interleaved boost converter and flat solenoid coupler," *IEEE Trans. Power Electron.*, vol. 36, no. 4, pp. 3894–3908, Apr. 2021.

[30] Y. Yao, Y. Wang, X. Liu, Y. Pei, and D. Xu, "A novel unsymmetrical coupling structure based on concentrated magnetic flux for high-misalignment IPT applications," *IEEE Trans. Power Electron.*, vol. 34, no. 4, pp. 3110–3123, Apr. 2019.

[31] M. Wang, J. Feng, Y. Shi, and M. Shen, "Demagnetization weakening and magnetic field concentration with ferrite core characterization for efficient wireless power transfer," *IEEE Trans. Ind. Electron.*, vol. 66, no. 3, pp. 1842–1851, Mar. 2019.

[32] C. Zhu et al., "A magnetic field concentration enhanced I-shaped transmitter for DWPT system to achieve low power fluctuation," *IEEE Trans. Power Electron.*, vol. 39, no. 1, pp. 1690–1700, Jan. 2024.

[33] Y. Wang, P. Gu, Y. Yao, and D. Xu, "Analysis and design of cubic magnetic coupler for high distance-to-diameter ratio IPT systems," *IEEE Trans. Ind. Electron.*, vol. 69, no. 1, pp. 409–419, Jan. 2022.

[34] T. Kan, Y. Zhang, Z. Yan, P. P. Mercier, and C. C. Mi, "A rotation-resilient wireless charging system for lightweight autonomous underwater vehicles," *IEEE Trans. Veh. Technol.*, vol. 67, no. 8, pp. 6935–6942, Aug. 2018.

[35] Y. Wang, J. Mai, Y. Yao, and D. Xu, "Analysis and design of an IPT system based on S/SP compensation with improved output voltage regulation," *IEEE Trans. Ind. Inform.*, vol. 16, no. 5, pp. 3256–3266, May 2020.

[36] J. Mai, Y. Wang, Y. Yao, and D. Xu, "Analysis and design of high-misalignment-tolerant compensation topologies with constant-current or constant-voltage output for IPT systems," *IEEE Trans. Power Electron.*, vol. 36, no. 3, pp. 2685–2695, Mar. 2021.
[37] X. Qu, Y. Yao, D. Wang, S.-C. Wong, and C. K. Tse, "A Family of hybrid IPT topologies with near load-independent output and high tolerance to pad misalignment," *IEEE Trans. Power Electron.*, vol. 35, no. 7, pp. 6867–6877, Jul. 2020.
[38] W. Zhong, S. Zhang, M. Chen, and M. D. Xu, "Reconfigurable resonant topology linking two-, three-, and four-coil modes for WPT with large coupling range and fixed frequency," *IEEE Trans. Power Electron.*, vol. 37, no. 7, pp. 8713–8725, Jul. 2022.
[39] Y. Wang, X. Xie, Y. Zhou, and W. Huan, "Calculation and modeling analysis of mutual inductance between coreless circular coils with rectangular cross section in arbitrary spatial position," in *Proc. IEEE 5th Inf. Technol. Mechatron. Eng. Conf.*, Chongqing, China, 2020, pp. 1258–1267.
[40] W. G. Hurley, M. C. Duffy, J. Zhang, I. Lope, B. Kunz, and W. H. Wölfle, "A unified approach to the calculation of self- and mutual-inductance for coaxial coils in air," *IEEE Trans. Power Electron.*, vol. 30, no. 11, pp. 6155–6162, Nov. 2015.
[41] Q. Wang et al., "Inductive power transfer system with constant current-constant voltage charging tolerating misalignment based on multiobjective optimization for compensation topology," *IEEE Trans. Power Electron.*, vol. 40, no. 3, pp. 4581–4591, Mar. 2025.
[42] G. Li et al., "An integrated mutually compensatory dual receiver for AGV misalignment-tolerant IPT charging," *IEEE Trans. Circuits Syst. II, Exp. Briefs*, vol. 72, no. 1, pp. 313–317, Jan. 2025.
[43] X. Duan, W. Han, Y. Hu, H. Tian, J. Huang, and Z. Zhang, "Magnetic-field-editable wireless power transfer system with DD2 magnetic couplers for position detection and misalignment tolerance," *IEEE Open J. Power Electron.*, vol. 6, pp. 266–276, 2025.
[44] C. Rong et al., "Optimization design of resonance coils with high misalignment tolerance for drone wireless charging based on genetic algorithm," *IEEE Trans. Ind. Appl.*, vol. 58, no. 1, pp. 1242–1253, Jan./Feb. 2022.
[45] P. Darvish, S. Mekhilef, and H. A. B. Illias, "A novel S–S–LCLCC compensation for three-coil WPT to improve misalignment and energy efficiency stiffness of wireless charging system," *IEEE Trans. Power Electron.*, vol. 36, no. 2, pp. 1341–1355, Feb. 2021.
[46] H. Yuan et al., "A novel anti-offset interdigital electrode capacitive coupler for mobile desktop charging," *IEEE Trans. Power Electron.*, vol. 38, no. 3, pp. 4140–4151, Mar. 2023.
[47] B. Zou, Z. Huang, I.-W. Iam, and C.-S. Lam, "Tuning control against coupler parameter variations due to misalignment in an optimal-efficiency-tracking and constant-power-output IPT system," *IEEE Trans. Power Electron.*, vol. 40, no. 5, pp. 7500–7511, May 2025.
[48] P. Gu et al., "A magnetic field reconstruction scheme for inductive power transfer systems to cross metal appliances," *IEEE J. Emerg. Sel. Topics Power Electron.*, vol. 13, no. 1, pp. 1349–1360, Feb. 2025.
[49] Y. Xu, Y. Li, Y. Chen, W. Zhou, R. Mai, and Z. He, "A multiple-gain-reconfigurable-rectifier-based IPT system for battery multistage constant-current high-efficiency wireless charging," *IEEE Trans. Power Electron.*, vol. 39, no. 1, pp. 1853–1869, Jan. 2024.

Peng Gu (Member, IEEE) was born in Harbin, China. He received the B.S. degree from Huazhong University of Science and Technology, Wuhan, China, in 2015, the M.S. degree from China Electric Power Research Institute, Beijing, China, in 2018, and the Ph.D. degree from Harbin Institute of Technology (HIT), Harbin, China, in 2023, all in electrical engineering.

He has been a Faculty Member with Northeastern University (NEU), Shenyang, China, in electrical engineering, since 2023. He has been also a Postdoctoral Fellow with NEU in control science and engineering, since 2023. His current research interests include wireless power transfer, magnetic coupling structure design, power system analysis, electromagnetic transient analysis, and dc–dc converter.

Dr. Gu was the recipient of the 2024 IEEE TRANSACTIONS ON POWER ELECTRONICS First Place Prize Paper Award and also the recipient of the Outstanding Ph.D. Thesis Award from HIT, in 2023, and from China Energy Research Society, in 2024.

Mingda Gao was born in Liaoning Province, China, in 2002. He received the B.S. degree in electrical engineering and automation in 2025 from the College of Information Science and Engineering, Northeastern University, Shenyang, China, where he is currently working toward the M.S. degree in electrical engineering.

His research interests include wireless power transfer, power electronics, and magnetic coupling structure design.

Xianrui Zeng was born in Guangxi, China, in 1997. He received the B.S. and M.S. degrees in electrical engineering, in 2020 and 2022, respectively, from the Harbin Institute of Technology (HIT), Harbin, China, where he is currently working toward the Ph.D. degree in electrical engineering from the School of Electrical Engineering and Automation.

He is a Research Engineer with the Institute of Spacecraft System Engineering, China Academy of Space Technology. His research interests include wireless power and data transmission systems, magnetic coupling optimization for aerospace applications, with particular emphasis on high-efficiency energy transfer solutions for spacecraft systems.

Shibo Wang was born in Liaoning Province, China, in 2000. He received the B.S. degree in electrical engineering and automation from Liaoning Technical University, Fuxin, China, in 2022. He is currently working toward the M.S. degree in electrical engineering with the College of Information Science and Engineering, Northeastern University, Shenyang, China.

His current research interest includes wireless power transfer.

Yijie Wang (Senior Member, IEEE) was born in Heilongjiang Province, China, in 1982. He received the B.S., M.S., and Ph.D. degrees in electrical engineering from Harbin Institute of Technology, Harbin, China, in 2005, 2007, and 2012, respectively.

From 2012 to 2014, he was a Lecturer with the Department of Electrical and Electronics Engineering, Harbin Institute of Technology. From 2014 to 2017, he was an Associate Professor with the Department of Electrical and Electronics Engineering, Harbin Institute of Technology. Since 2017, he has been a Professor with the Department of Electrical and Electronics Engineering, Harbin Institute of Technology. His research interests include wireless power transfer, dc–dc converters, soft-switching power converters, power factor correction circuits, digital control electronic ballasts, and LED lighting systems.

Dr. Wang is an Associate Editor for IEEE TRANSACTIONS ON INDUSTRIAL ELECTRONICS, IEEE JOURNAL OF EMERGING AND SELECTED TOPICS IN POWER ELECTRONICS, IEEE ACCESS, *IET Power Electronics*, and *Journal of Power Electronics*.